4 Heat flux measurements using single-layer thin film gauges

4.1 Introduction

Heat flux measurements were carried out on the second stator of the VKI Brite one and a half stage turbine at 50% of the blade height (test section of the VKI I.L.P. facility, CT3). The purpose was to measure heat transfer distributions around the second stator profile and report them under the form of a Nusselt number based on the blade chord, *C*, and defined as:

$$Nu = \frac{hC}{k_{GAS}} = \frac{Q_W C}{k_{GAS}\left(T_{GAS} - T_W\right)} . \tag{30}$$

The measurement technique is the thin film gauge that allows to derive a wall heat flux (Q_W) from a measured wall temperature history (T_W) when testing in a short duration blowdown windtunnel. The gas temperature (T_{GAS}) is evaluated by means of a thermocouple and k_{GAS} stands for the conductivity of the gas.

The tests are performed using two different kinds of thin film gauges: the single and two-layer gauges. The measurement chain is described and the flow field is explained thanks to the conclusions drawn from the single-layer gauge results. The results from the two-layer gauges are then compared with those from the well validated technique of single-layer gauges in chapter 5.

4.2 Measurement locations and test conditions

4.2.1 Measurement locations

The second stator mid-span section is instrumented at 24 locations with single-layer thin film gauges. The additional measurements carried out with the two-layer gauges array covered 12 locations. All the measurements that are analyzed in this chapter were performed on the second stator of the one and a half stage turbine (see Figure 4-1).

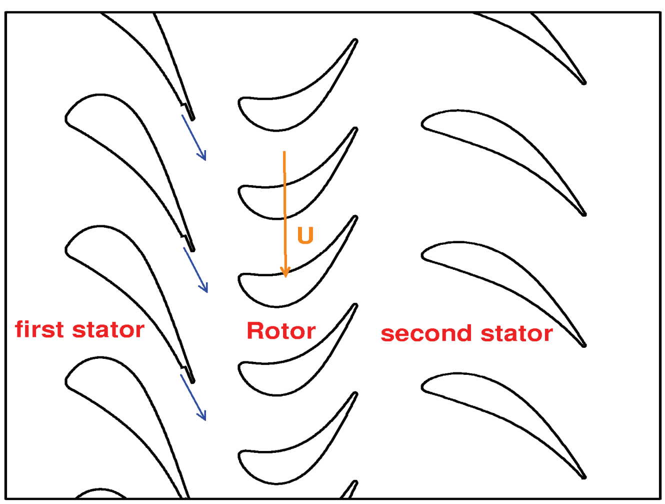

Figure 4-1: Blade to blade representation of first stator, rotor and second stator

In the following paragraphs, the gauges will be referred with a three digit number under the form *zyx* where *z=2* for single-layer gauges and *z=5* for two-layer gauges. *yz* is the index of the gauge between *01* and *24*. The position of each gauge on the curvilinear coordinate system of the blade contour at 50 % span is reported in Table 4-1. In Figure 4-2, the two-dimensional blade contour is shown, where the positions of the gauges are clearly indicated.

Single-layer Gauge	Two-layer Gauge	S/ S $_{MAX}$	Single-layer Gauge	Two-layer Gauge	S/ S $_{MAX}$
201		-0.954	213		0.052
202		-0.834	214	514	0.103
203		-0.704	215	515	0.169
204		-0.580	216	516	0.234
205	505	-0.390	217	517	0.307
206	506	-0.272	218	518	0.384
207	507	-0.157	219	519	0.481
208	508	-0.086	220		0.580
209		-0.042	221		0.675
210		-0.022	222		0.766
211	511	-0.003	223		0.847
212		0.016	224		0.934

Table 4-1: Position of the gauges on the blade contour

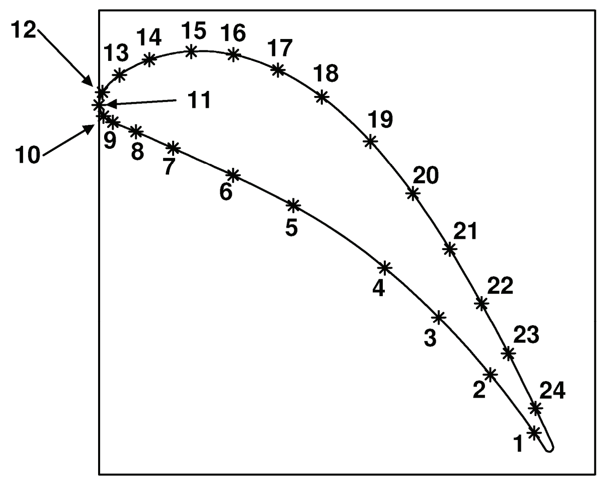

Figure 4-2: Position of the gauges in two dimensional representation

4.2.2 Test conditions

The turbine operating conditions are summarized in Table 4-2. The temperature T_{01} is measured with a reference thermocouple placed in front of the first stator and its average value from eighteen tests (Table 18-2) is found equal to *472.4K*. A traverse of four heads thermocouple probe is used for the T_{03} temperature measurements, in front of the second stator. The temperature T_{04} is also measured with a reference thermocouple placed behind the second stator. The inlet and outlet Reynolds number to the second stator are equal to *520,000* and *480,000* respectively.

There are test-to-test variations, i.e. the stage inlet total pressure and total temperature change slightly. For this reason, the second row of Table 4-2 indicates the dispersion (20:1) on the different measurements. This dispersion is computed using the data from eleven similar tests assuming that the distribution of the conditions is Gaussian. As a result, the dispersion can be computed by multiplying the standard deviation by *1.96* that provides *95%* of the events (or (20:1)) (Arts, 1994). Of course, if T_{01} and P_{01} change from test to test, the rotor and the second stator exit conditions will change accordingly. For this reason, the exit conditions are reported as ratio to the inlet conditions. The second part of Table 4-2 provides typical mean absolute values of the flow parameters computed by the ratios of the first part of Table 4-2 and the mean stage inlet conditions.

The second stator inlet Mach number is *0.43* and the flow inlet angle is supposed to be *13 deg*, as measured in a single stage configuration. At the second stator exit, the Mach number is *0.68*. The exit angle is assumed to be *56 deg* (design value). The turbine stage inlet turbulence is *1.8 %*. All the tests are performed at a nominal speed of *6500 RPM* with coolant flow ejected from the front stator vanes trailing edge.

For the second stator, an average wall temperature of *293 K* results into a gas to wall temperature ratio of *1.19*, or to a temperature difference that drives the heat transfer of only *57 K* while for the first stator it would be *179 K*. This means that both the gas temperature and the wall temperature must be measured very carefully for accurate Nusselt number calculations (Eq. (30)).

	P_{01} [bar]	T_{01} [K]	P_{03}/P_{01}	T_{03}/T_{01}	P_{04}/P_{01}	T_{04}/T_{01}	T_{04}/T_{03}
Mean	2.231	472.4	0.376	0.769	0.362	0.741	0.963
Disp +/- (20:1) [%]			1.8	2.3	1.9	2.1	

	P_{01} [bar]	T_{01} [K]	P_{03} [bar]	T_{03} [K]	P_{04} [bar]	T_{04} [K]	
Mean	2.231	472.4	0.839	363.3	0.808	350.0	
Disp +/- (20:1)			0.015	8.3	0.015	7.3	

Table 4-2: Turbine operating conditions

4.3 Single-layer thin film gauges: operating principle

4.3.1 Thermal products calibration

Whatever data reduction technique is chosen to derive heat flux from wall temperature measurements, the knowledge of the thermal product $\sqrt{\rho c k}$ is of primary importance (paragraphs 3.3 and 3.4). The wall heat flux Q_W of Eq. (30) can be rewritten as a function of the wall temperature T_W :

$$Q_W = \frac{\sqrt{\rho c k}}{\sqrt{\pi}} f\left(T_W, t\right) . \quad (31)$$

The values of the thermal products of the different materials are given in Table 4-3. The substrate of the single-layer gauges is Macor and the calibration was performed by means of the electrical discharge method. Note that the substrates of the two-layer gauges, whose results are discussed in paragraph 5.2, are Upilex (top layer) and conventional steel (material of the blades). The thickness of the Upilex layer that is used for the heat flux calculations is $175 \cdot 10^{-6}\ m^*$. (More information about the calibration techniques can be found in chapter 3).

Material	Thermal Diffusivity (α) (10^{-6}) m^2/s	Specific Heat (k) W/(mK)	Thermal product $(\rho c k)^{1/2}$ J/($m^2 K s^{0.5}$)
Macor	0.797 ***	1.851 **	2073.5 *
Upilex	0.1698 ***	0.288 **	699 *
Steel	4.881 ***	18 **	8147 *

Table 4-3: Thermal products

*** calculated values
** nominal values
* calibrated values, see Table 3-1

4.3.2 Temperature resistance calibration

The average value of the sensitivity to temperature (a_T in Eq. (2)) for the single-layer gauges is $a_T = 0.00241K^{-1} \pm 4.3\%$ and for the two-layer is $a_T = 0.00306K^{-1} \pm 1.1\%$. (The individual values of a_T for each thin film are shown in Table 18-3 and in Table 18-4.) Note that R_0 and T_0 are reference values and for our case $T_0 = 289.8\ K$. The bulk material value for the platinum is $a_T = 0.00301K^{-1}$ (material of the thin film of the single-layer gauges) and for the nickel is $0.0054\ K^{-1}$ (material of the thin film of the two-layer gauges, see Denos, 1996). Note that for both types of gauges, the value of the calibration is quite far from the bulk material one. The later either results from the manufacturing procedure when the metallic thin film is deposited onto the gauge substrate, or is a property of the thin layer (only few µm) when compared to the bulk properties.

4.3.3 Calibration of the boards

Dedicated electronic boards are used in the rig. Because the mean value of the resistance (typically $60\ \Omega$) is large with respect to the variation that the gauge will experience during the blowdown (typically $1\ \Omega$), the board can operate under two modes of amplification (Denos, 1996).

In the first mode, called R_0, the overall resistance of the gauge is measured with a gain a_{R0}~$0.010\Omega/V$ ($R_0 = a_{R0}V + b_{R0}$). This is performed just before the blowdown in order to know the initial temperature distribution of the blade. Indeed, the second stator is preceded by a rotor that generates ventilation. The heat produced causes a non-uniform temperature distribution around the second stator, prior to the measurement.

In the second mode, called ΔR, the Wheastone bridge is balanced in such a way that the output becomes zero for the initial value of the resistance and the gain of the amplifier is multiplied by 50 ($a_{\Delta R} \sim 0.5\ \Omega/V$, $\Delta R = a_{\Delta R}V + b_{\Delta R}$), so that small variations can be resolved with measurable changes of voltage. The 'auto-zero' and the gain switch are performed just before the blowdown.

Three distinct boards are used with 6 channels each. Each channel is calibrated in the two modes as shown in Table 18-6. While the first digit refers to the board, the second digit refers to the channel of a board. Each gauge is connected to a specific Wheatstone bridge of one of the three boards as shown in Table 18-5.

4.3.4 Signal conditioning

In the following experiments, two aspects at different time scales are resolved:

a) the time-averaged Nusselt number distribution i.e. a mean value computed over the useful test duration (~0.3 s),

b) the time-resolved variations i.e. fluctuations caused by blade passing events.

Because the fluctuations are small compared to the mean value, a special signal conditioning is used in order to resolve properly both quantities. The transfer function between the wall temperature and the wall heat flux is $1/\sqrt{j\omega}$ (Eq. (7)). This means that sinusoidal fluctuations of heat flux of a given amplitude will cause small wall temperature fluctuations at high frequency and large fluctuations at low frequency. For this reason, when operating in ΔR mode, Ainsworth et al. (1989) suggested that the board amplifies in a different way high and low frequency fluctuations. This modulation of the gain as a function of frequency is performed by means of a combination of resistances and capacitors. During the signal conditioning of the time-resolved periodic measurements in the CT3 facility the amplification is somehow proportional to the square root of frequency between *100Hz* and *20kHz*.

4.3.5 Data acquisition

Because the resolution of the data acquisition system is limited to 12 bits (4096 levels) and because data must be recorder at two time scales (blowdown duration *~0.2 s* and blade passing frequency i.e. *6500 RPM/60*64 = 6933 Hz*), the signal is finally shared in two components. For the time-averaged quantities, the signal is low pass filtered at *750 Hz* and sampled at *1.2 kHz* (During the data reduction, it is further numerically low pass filtered at *100 Hz*). For the time-resolved quantities, the signal is high pass filtered at *100 Hz* in order to remove the mean value and amplified by a factor of *10* before being sampled at *300 kHz*. (Further high pass filtering at *750 Hz* is performed during the data reduction.)

4.3.6 Demodulation

Before being able to process the data, the inverse transformation $H^{1}(\omega)$ must be applied to the measured voltage V_{MOD} in order to recover the value of the voltage that enters the board V_{DEM}. This demodulation must be applied to both low pass filtered and high pass filtered components of the signal.

Regarding the low pass filtered component, an approximation of the gain $|H^{1}(\omega)|$ in the Laplace domain can be given from two first order systems (see coefficients in Table 4-4). The inverse transformation and its approximation with two first order systems are described in the Eq. (32), (33):

$$\overline{V}_{DEM} \rightarrow \{H(\omega)\} \rightarrow \overline{V}_{MOD} \quad \text{or} \quad \overline{V}_{MOD} \rightarrow \{H^{-1}(\omega)\} \rightarrow \overline{V}_{DEM} \ , \tag{32}$$

$$H^{-1}(\omega) = \sum_{i=1}^{2} \frac{b_i}{1 + a_i e^{-j\omega}} \qquad \omega = 2\pi f \ . \tag{33}$$

$f_{CUT1} = 2.62$ $f_{CUT2} = 192.37$ $g_1 = 0.884$ $g_2 = 0.117$ $f \sim 0.1 - 100$ Hz	$\tau_{1,2} = \dfrac{1}{2\pi f_{CUT1,2}} \quad a_{1,2} = \dfrac{\Delta t - 2\tau_{1,2}}{\Delta t + 2\tau_{1,2}} \quad b_{1,2} = 1 + a_{1,2}$

Table 4-4: Coefficients of the two linear systems used as approximation for $|H^{-1}(\omega)|$ (Ferrara, 2002)

And in the time domain all the above analysis can be summarized in one equation, where *n* is the index for the discretization of time.

$$V_{DEM}^{n+1} = g_1\left(b_1 V_{MOD}^{n} - a_1 V_{DEM}^{n}\right) + g_2\left(b_2 V_{MOD}^{n} - a_2 V_{DEM}^{n}\right) . \tag{34}$$

The concept of the demodulation of board 3 is similar with the one of the boards 1 and 2, but in this case, the amplification for less than *100 Hz* is practically constant. Considering that the signal is also numerically low pass filtered at *100 Hz*, the demodulation of the steady component with board 3 does not really influence the demodulated signal.

For the time-resolved quantities, the inverse transfer functions $H^{1}(\omega)$ of the boards in the Laplace domain is directly used for the demodulation of the signal, because their transfer functions $H(\omega)$ can not be approximated by two first order systems for higher frequencies.

The Fast Fourier Transformation (FFT) of the modulated signal is multiplied by the inverse transfer function in the Laplace domain (complex multiplication), which generates the FFT of the demodulated signal. Then an inverse FFT of the latter signal will produce the demodulated signal in the time domain.

Furthermore, in our case the demodulated signal is also filtered between the limits of 1 *kHz* and 40 *kHz*. This filtering is performed by setting the amplitude of the spectrum to a very low value under 1*kHz* and over 40*kHz*. An inverse FFT is performed to recover the signal in the time domain. Finally, the signal is divided by a factor *10* to counteract the amplification during acquisition.

The signal conditioning, the data acquisition and the principles of the signal demodulation were both established by Denos (1996).

4.4 General description of the data processing procedure

4.4.1 Introduction

For the thin film gauge measurement technique, the heat exchange by convection around the blade profile is determined by the conductive wall heat flux on the blade surface. More specifically, the Nusselt number distribution *Nu* depends on the heat transfer coefficient *h*, which is proportional to the convective heat flux Q_C and inversely proportional to the temperature difference between the gas temperature T_{GAS} and the gauge temperature T_W, at the different points of the blade profile:

$$Nu = \frac{hC}{k_{GAS}} = \frac{Q_C C}{k_{GAS}\left(T_{GAS} - T_W\right)} \quad . \tag{35}$$

The convective heat flux, on the blade surface, Q_C, should be equal to the conductive wall heat flux on the same surface, Q_W. The latter can be easily calculated if the unsteady heat conduction in the blade is solved for each time step (chapter 3). Note that k_{GAS} is the thermal conductivity of the gas near the surface of the blade.

As far as the steady component is concerned for a limited data reduction time, *40ms*, far enough from the beginning of the test, the gas temperature is considered constant.

4.4.2 Time-averaged component

Figure 4-3 shows a typical trace of recorded voltage during the test (raw signal). The blowdown lasts around *0.3 s*. The R_0 mode (paragraph 4.3.3) corresponds to the region around the point *P1*. Then the rest of the signal corresponds to the ΔR_0 mode. Note that for this series of experiments, there is no ejection of cold air (coolant) from the stator vanes (region after *P3* and just before *P4*). In the first graph, the demodulated signal is shown after being filtered at *100 Hz*. The shutter valve opens when the signal starts rising (point *P4*). A temperature increase (ΔT_W) that can be coarsely approximated to a signal proportional to the square root of time (second graph) is observed due to the step like evolution of the gas temperature. Then a temperature decrease occurs after the end of the test. The corresponding wall heat flux (Q_W) is calculated from the one dimensional unsteady conduction in the vane (third graph). For the calculation of the Nusselt number (Eq. (35)), average values of gas temperature, wall temperature and heat flux are taken between points *P5* and *P6*. This region is close to the end of the test and seems to be the most repeatable part of the signal from test to test.

4.4.3 Time-resolved component

4.4.3.1 Important numbers in phase locked average

The nominal rotational speed of the rotor is *6500 RPM* or *6500/60 Hz*. The total number of rotor blades is *64*, so the blade passing frequency should be *6500/60*64 Hz*. The data reduction is based on three revolutions of the rotor, so in total there are *3*64 = 192* blade passing events. The sampling frequency is *300 kHz*, thus there are *300000 / (6500/60*64)=43* points to describe the recorded signal per blade passing period. Each time period, which corresponds to the blade passing frequency, is split into smaller time differences called classes in the non-dimensional base when a phase locked average (*PLA*) on the recorded signal is performed. It would be preferable to have at least one point in each class of every period, so the choice of the number of classes is equal to *300000 / (6500/60*64)*. This means that in three rotor revolutions, every class has an average of *192* points. Note that the phase locked average eliminates all the fluctuations that are not multiple of the blade passing frequency. In practice the evolution of the rotational speed is linear with time. The knowledge of the above law defines precisely the limits in time corresponding to one blade passing period in space.

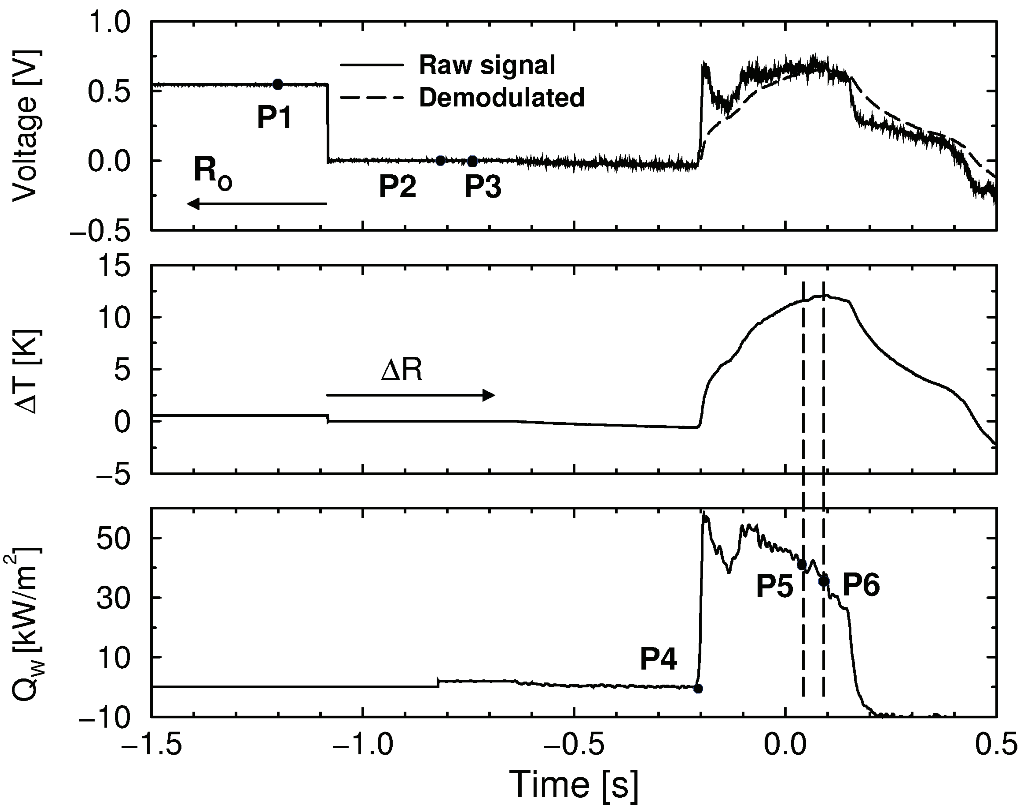

Figure 4-3: Heat flux calculation for the time-averaged component

4.4.3.2 Phase correction

The location of the rotor relative to the location of the two stators is known at every time step of the tests, by means of a system of 64 pulses. On the rotor disk, there are 64 holes in total and one of them is larger than the others. Then each time that a constant LASER beam passes through the hole, a pulse is generated. One of the 64 pulses is always larger than the others. Then the position of the large hole is well known.

The *PLA* starts at the same relative position of the rotor to the second stator for all the gauges (when the large pulse is measured close to the nominal speed of the rotor *6500 rpm*), although the 24 single-layer gauges are situated in three different vanes of the second stator (see Figure 4-4). In addition, there is no relative position between a rotor blade and a stator vane that is the same more than once at the same time per revolution; the total number of the rotor blades is *64* and of the stator vanes is *43*. A technique to obtain the same relative position between the three different combinations of blades and vanes is to shift the *PLA* to the time phase of the rotor in such a way that for each combination the axis of blades of the rotor to be aligned with the axis of the vanes of the second stator. Thus, in total, it is necessary to introduce three different relative time shifts coherent to each other. For this reason, the shift corresponds to the relative time between the blade of the rotor just before the corresponding vane of the stator. Note that the coherence of the three shifts impose a difference between them such as *(64/43 – 1) = 0.488* (the number of blades over the number of vanes minus 1, so that the shift is less than one rotor period in the relative phase of rotor).

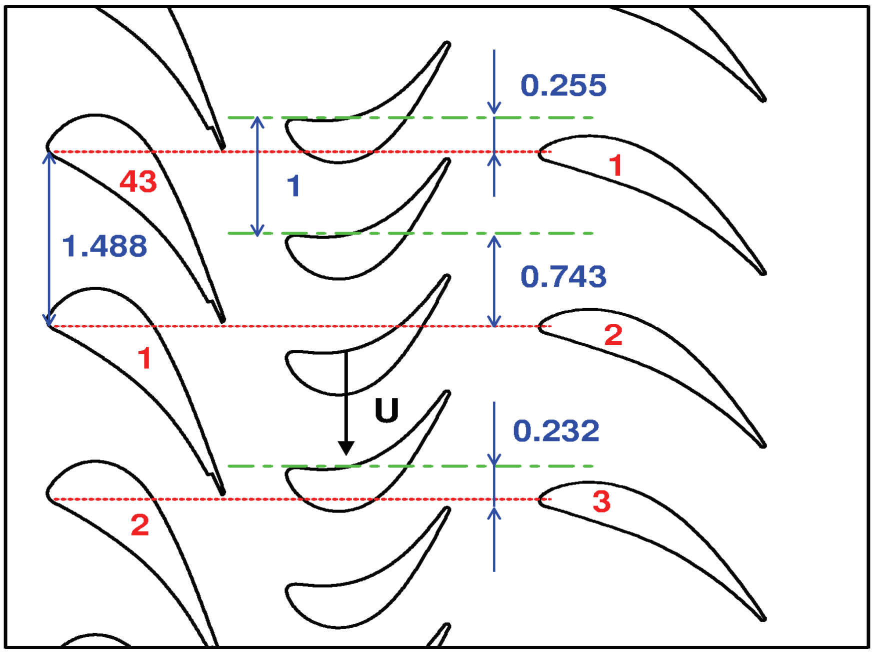

Figure 4-4: Relative time for the axis of blades of the rotor to be aligned with the axis of the vanes of the second stator expressed in phase of the rotor

4.4.3.3 Random unsteadiness on the signal

The correlation coefficient and the *RMS* are additional indicators that quantify the random unsteadiness existing in the signal. In particular, the correlation coefficient is the coefficient that shows the quality of the linearity between the raw signal and the *PLA* for the range of the *192* periods. Thus, the closer to 1 is the correlation coefficient, the more periodic is the signal. This coefficient characterizes the shape of the signal. It is insensitive to scale factor or to a shift in amplitude and is slightly sensitive to phase shift and is relatively insensitive to peaks.

More information about the *PLA* technique, the phase correction of the *PLA*, as well as the correlation coefficient and the *RMS* definition can be found in Denos (1996).

4.5 Time-averaged component of the single-layer gauges

4.5.1 Geometrical parameters of the blade profile

The parameters concerning the description of the blade profile are shown in Figure 4-5. The results are shown as a function of the non dimensional curvilinear abscissa of the gauges, S/S_{MAX}, where S is the curvilinear abscissa starting from the leading edge (L.E.) around the blade profile either on the suction side (S.S.) or the pressure side (P.S.) of the blade and finishes at the blade trailing edge where $S=S_{MAX}$. On the same graph, the chord C and the axial cord C_{AX} are also indicated.

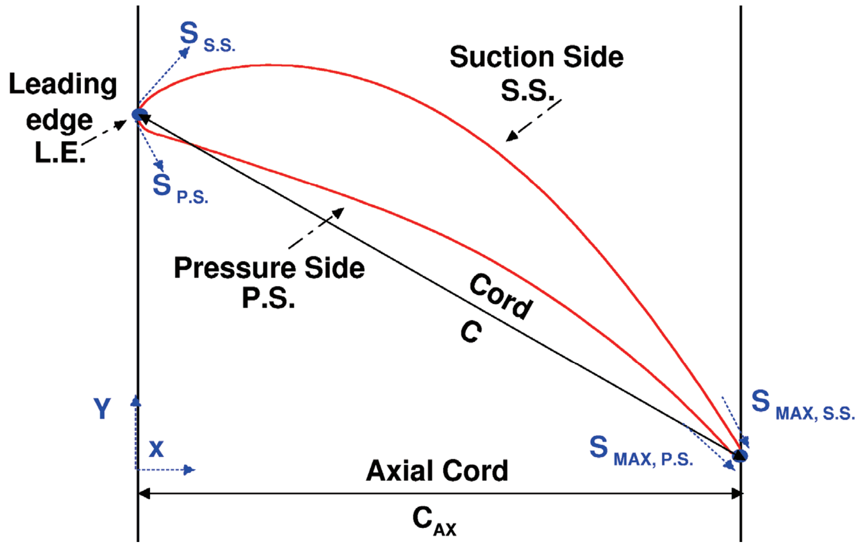

Figure 4-5: Parameters of the balde profile

4.5.2 Initial temperature distribution

The initial temperature of the blade before the run-up may be higher than the ambient temperature, in the case of successive tests. In Figure 4-6, the temperature distribution prior to the blowdown along the blade is shown as a function of the non dimensional curvilinear abscissa of the gauges, S/S_{MAX}, for five successive measurements performed during the same day. As the testing progresses, the turbine gets hotter and hotter and this is felt on the second stator initial temperature distribution. Note that the shape of this distribution is similar for all the tests. The mean level of temperature could also be a function of the duration of the run-up (duration of ventilation) as well as a function of the pressure level in the test section during the ventilation but this did not appear to be predominant in our case.

Owing to the proximity of the leading edge of the second stator with respect to the rotor, higher temperatures are observed in this region. More specifically, the gauge 213 is the one that has the highest initial temperature, and not the gauge 211, which is closer to the stagnation point. (The position of the gauges is shown in Figure 4-2.) This seems logical since the windage flow is directed to the suction side of the second stator (see Figure 4-1).

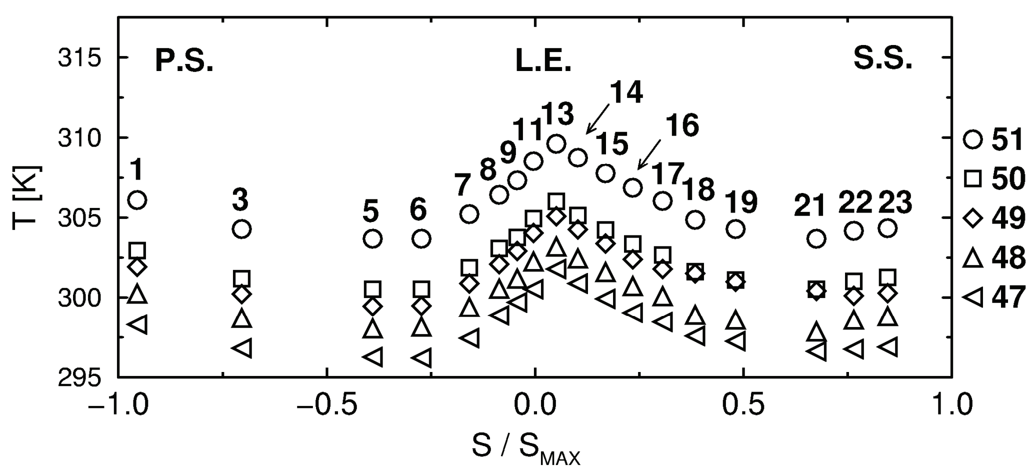

Figure 4-6: Initial temperature distribution at 50% span

4.5.3 Nusselt number calculations

In Figure 4-7, the averaged values of the blade wall temperature increase during the blowdown, the corresponding wall heat fluxes and Nusselt numbers are given, for five tests of 18 single-layer gauges. The gauge 211, which is the closest to the leading edge, is the one that feels the maximum wall temperature increase and heat flux during the test, because of the lack of insulation from any boundary layer. Then both temperature and heat flux decrease rapidly as the boundary layers develop on suction and pressure sides. Furthermore, it can be noticed that although the average wall temperature increases for each gauge from one test to the previous one, the average wall heat flux is decreasing in such a way that the Nusselt number of each gauge takes the same value for all the tests; this is coherent with the increase of mean level of the temperature during the successive tests and with the definition of the non-dimesional Nusselt number. (Note that the gas flow is the same from test to test.) The highest differences on the Nusselt number are found in the stagnation region at the gauge 211.

In Figure 4-6 and Figure 4-7, the total number of presented gauges is 18 and not 24. The reason is that 5 repeatable tests exist only for these 18 gauges and only one test is acquired for the last 6 gauges. The mean Nusselt number of the 18 gauges together with the Nusselt number of the last 6 gauges is presented in the top graph of Figure 4-8.

In the bottom graph of Figure 4-8, the repeatability of the Nusselt number of the single-layer gauges (±*103*) is indicated in red bars and is calculated on the basis of in total 5 tests on 17 single-layer gauges, (85 values). The gauge number 211 gives very high differences from test to test, and is not used for the calculation of the repeatability.

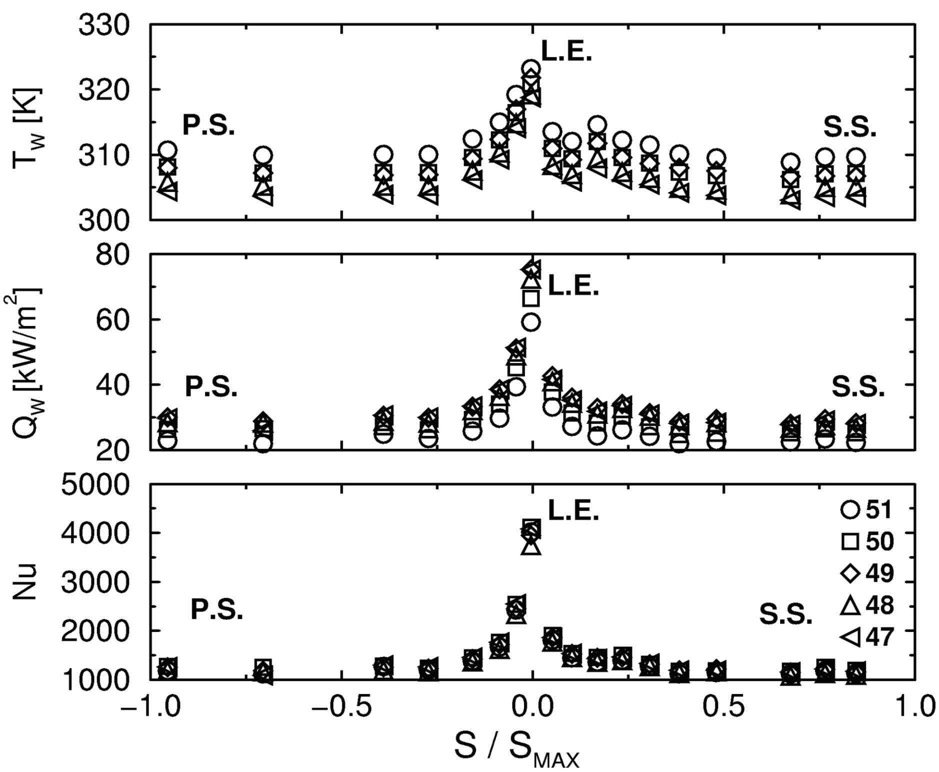

Figure 4-7: Wall temperature, heat flux and Nusselt number distribution at 50% span for the 18 single-layer gauges for five repeatable tests

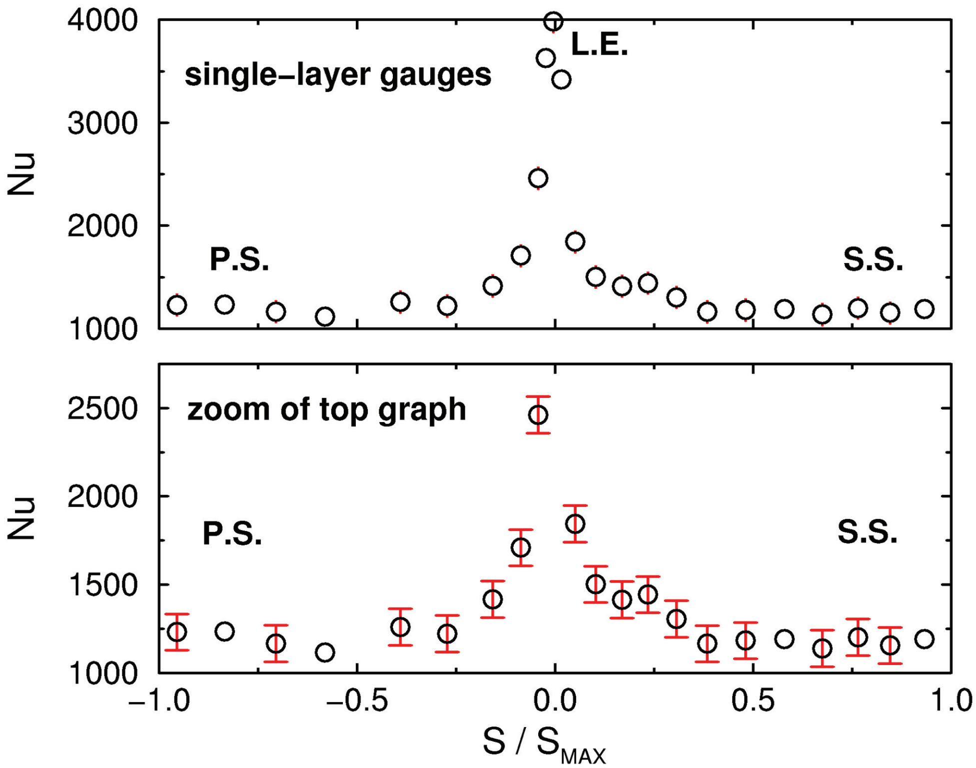

Figure 4-8: Nusselt number distribution at 50% span for the single-layer gauges

4.6 Time-resolved component of the single-layer gauges

4.6.1 Periodicity of the raw signal

This section focuses on the phase locked average traces of the Nusselt number. The Nusselt number is calculated in the same way it was done for the steady component: the raw signal is demodulated, converted into temperature and into flux. The flux is then phase locked averaged. The FFT of one typical demodulated signal is shown in Figure 4-9 .The blade passing frequency is clearly visible as well as five harmonics. The resolution in frequency is *18.31 Hz*.

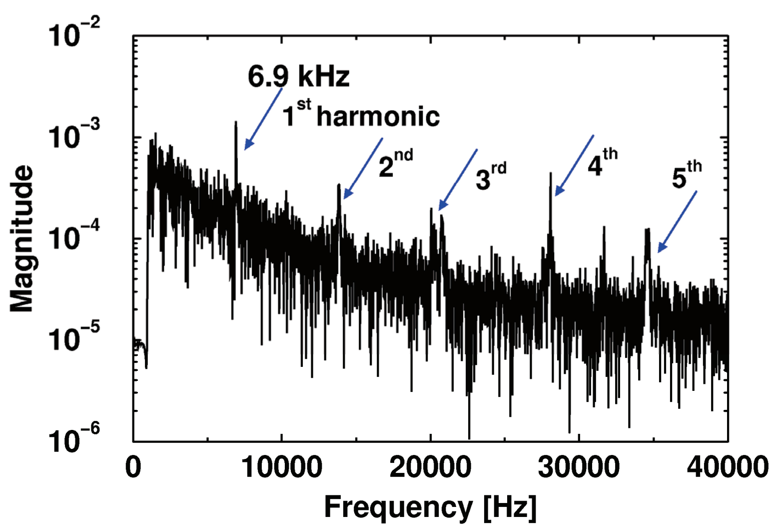

Figure 4-9: FFT on the demodulated voltage signal of gauge 511

4.6.2 Nusselt number phase locked average

In order to assess the repeatability of the measurements, the Nusselt number traces of two gauges (17 and 6, see Figure 4-2) are shown in Figure 4-10 as a function of the phase locked time on the rotor blade passing events, Φ_{rotor}, for five different tests. For the time period $\Phi_{rotor} = 0$ till $\Phi_{rotor} = 1$, the rotor performs an angular displacement equal to one rotor pitch. The dominant phenomenon of the flow pressure and temperature perturbations on gauge 17 results not only in a higher Nusselt number amplitude but also in a better repeatability in comparison to the Nusselt number traces of the gauge 6, where the unsteadiness of the flow is the main component.

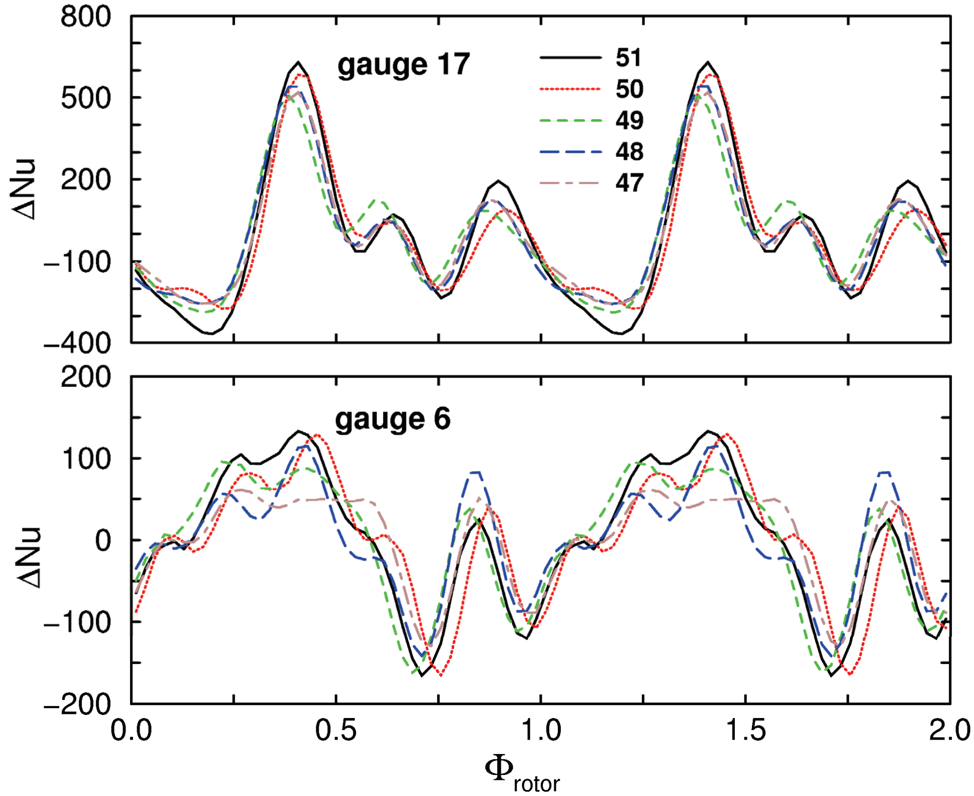

Figure 4-10: Nusselt number traces of two gauges of five different measurements for the single-layer gauge

The minimum-maximum envelope of the phase locked-average, the mean *RMS* and the correlation coefficient at 50% span are plotted in Figure 4-11. In order to cover the 24 measurement locations, two tests were required (test number 51 with 18 gauges and test number 45 for the last six gauges). The minimum-maximum envelope corresponds to the lowest and highest amplitudes of the Nusselt number fluctuations, whose mean values are set equal to zero; it indicates a large region on the suction side where the differences between the maximum and the minimum values of Nusselt number are high. For the same time and region, the mean RMS values are low, while the correlation coefficient could be considered to be almost constant. Therefore, there is a periodic phenomenon on that region of the blade.

This periodic phenomenon is probably of potential nature. The relative exit Mach number of the rotor blades being around *0.9*, a rotor trailing edge steady shock is not expected but the rotor static exit pressure field is probably significantly distorted. As the rotor operates in the transonic regime, instantaneous shocks that create potential flow fluctuations can be possible in the relative frame. More specifically, these instantaneous shocks are characterized by a steep gradient in both static pressure and temperature. Then the generated steep total pressure and temperature gradients in the absolute frame are the image/trace of their corresponding static quantities, since the absolute exit Mach number of the rotor is only *0.42*. Thus, the steep gradient on the Nusselt number fluctuations (at rotor phase Φ_{rotor} after *0.25* and *1.25* – see Figure 4-10) can be generated by the steep gradients of the flow total conditions. The periodic traversing of the non-uniform potential field occurs at the peripheral speed of the rotor. In addition, there is only one large Nuselt number oscillation per rotor blade, which suggests that the rotor wake is at least one order of magnitude smaller. Unsteady total pressure and temperature measurements downstream of the same rotor performed by Paniagua et al. (2001) suggested that there is no clear evidence of the rotor wake. Steady and unsteady static pressure measurements along the second stator blade at 15%, 50% and 85% span performed by Gadea et al. (2004) revealed additional information on the flow field around the second stator.

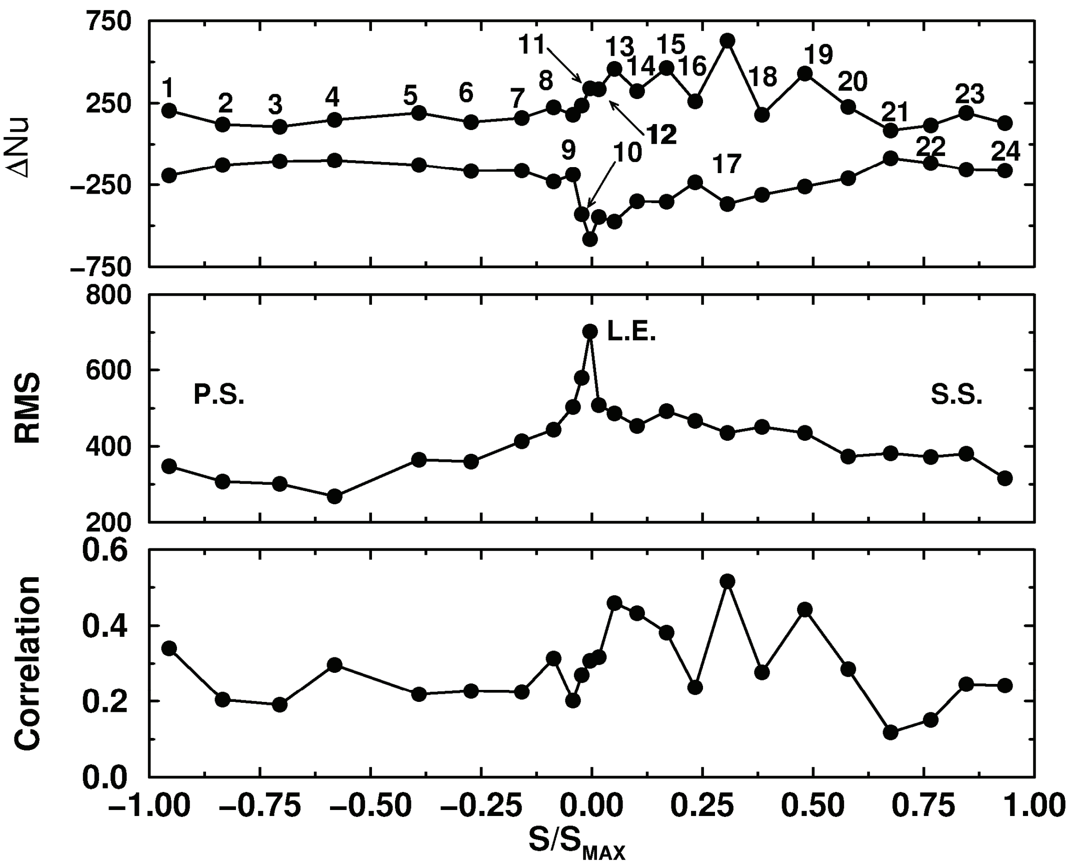

Figure 4-11: Statistics for unsteady Nusselt number at 50% span

By similarity with transonic blade rows (e.g. Denos et al., 2000), the direction of propagation of this non-uniformity is expected to be between *0°* and *20°* from the horizontal direction (see schematic in Figure 4-12). Consequently, the region of the suction side where gauges 15, 16 and 17 are located will be influenced first. As a result, one would expect that this perturbation moves upstream towards the leading edge (gauge 11).

This appears more clearly in the traces of the Nusselt number plotted over two blade-passing periods, in Figure 4-13. Each graph represents the 24 single-layer gauges, starting on the pressure side, going from the trailing edge towards the leading edge (gauges 1 to 11) and then on the suction side from the leading edge towards the trailing edge (gauges 11 to 24). The mean value of each fluctuation is zero but the curves are simply shifted by a constant value for clarity. The highest (or lowest) amplitudes are identified at gauges 11, 12, 13, 14, 15 and 17 and they seem to move upstream from gauge 17 to gauge 11. This information can easily be explained from the flow pressure and temperature perturbations coming from the rotor blades.

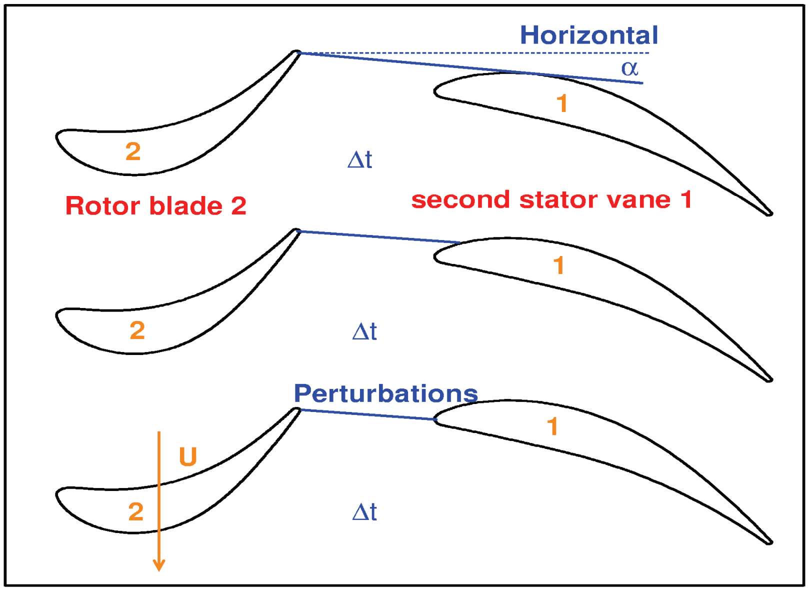

Figure 4-12: Pressure perturbation sweeping from the rotor blades to the suction side of the stator vanes close to the region of gauges 15, 16, 17

The representation of the movement of the flow perturbations on the Nusselt number traces (shown in purple, red and blue in Figure 4-13) validates once more the idea that these perturbations are the reasons of the high amplitudes on the Nusselt number traces. If no other unsteady phenomena would occur in the flow and if the disturbances move perfectly with the peripheral speed of the rotor, then the time *dt* to move one perturbation from one gauge to the next one is described in the next set of equations:

$$\Delta t = \frac{\Delta y}{U}, \quad \Delta y = y'_{i-1} - y'_i, \quad W = 2\pi \frac{\Omega}{60} \cos \alpha R_{MID}, \quad y'_i = y_i \cos \alpha + x_i \sin \alpha , \qquad (36)$$

where x_i, y_i stand for the coordinates of the *i* gauge, *a* for the angle of perturbations, *Ω* for the rotational rotor speed in *RPM*, R_{MID} for the rotor radius at midspan, *u* for the propagating speed of the perturbations.

The time *dt* can be easily transformed into phase on the rotor blade passing period. Then these phase traces are shifted by a constant value each time so that are plotted on the Nusselt number traces; then the curves that show the movement of the pressure perturbations dependent on their angle are formed. The three colored lines in Figure 4-13, correspond to *α* equal to *0*°, *10*°, *20*° as one sees them from left to right. Any different value of *α* in between *0*° and *20*° is in between the two outside cross lines. Note that as the angle of perturbations augments, the first influenced gauge moves from number 15 (for *0*°) to 17 (for *20*°). Gadea et al. (2004) suggested a value for *a* equal to *8*°.

Also, the minimum Nusselt number traces of the gauges (from 10 till 17), which are mainly influenced by the flow perturbations, follow better the *10*° line that describes the movement of the perturbations. For the rest of the gauges, the Nusselt number amplitudes get very low and new oscillations appear, which can be explained by the very high unsteadiness of the flow field together with the fact that the flow perturbations are not as strong as for the case of a shock to propagate much further. Note that there is still the wake of the rotor blades coming on the vanes from a different angle, and the interaction between the wake and the pressure perturbations can introduce phenomena that are not easy to identify.

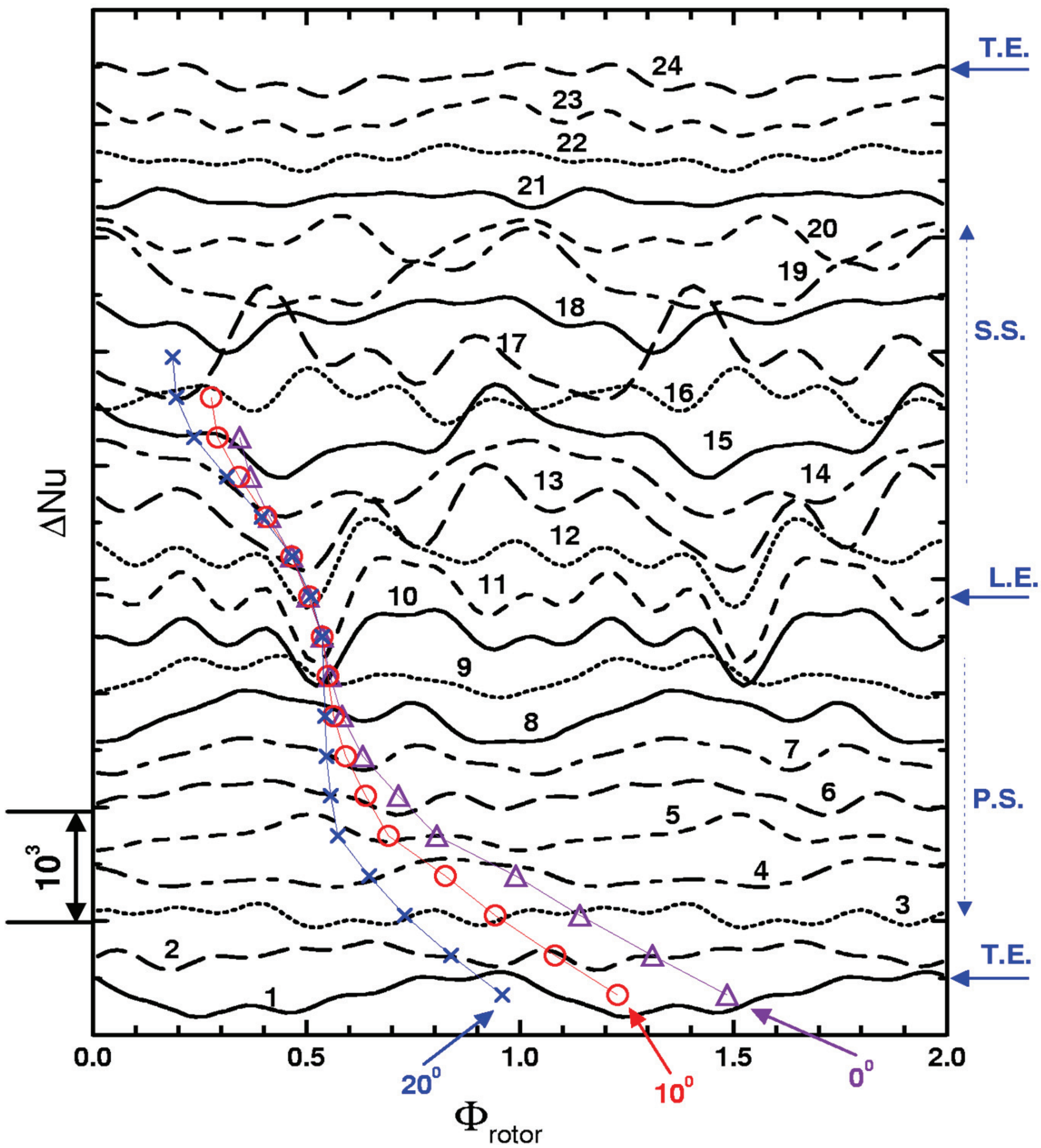

Figure 4-13: Unsteady Nusselt number traces at 50% span for the single-layer gauges combined with the traces of different angles of the flow pressure/temperature perturbations (0˚, 10˚, 20˚)

In case that the Nusselt number traces (for the gauges from 10 till 17) are shifted proportionally to the distance (dS) of the gauges on the blade curvilinear system from the leading edge (Figure 4-14), then the movement of the flow perturbations on the Nusselt number traces, shown by the red arrow, seems to propagate with a constant speed. The position of the minimum Nusselt number traces move linearly with the rotor phase.

The amplitudes of gauges 18, 19 and 20 are also considered quite high compared with the rest of the gauges in pressure and suction side of the vane. It seems that more complex phenomena occur in this region or more likely that the flow perturbations move downstream after the gauge 17. Note that the gauge 16 seems not to follow the same perturbations as its neighboring gauges. This can be due to the high unsteadiness of the flow; the noise level on the gauge, its correlation coefficient and its mean *RMS* was not higher than the ones on the other gauges.

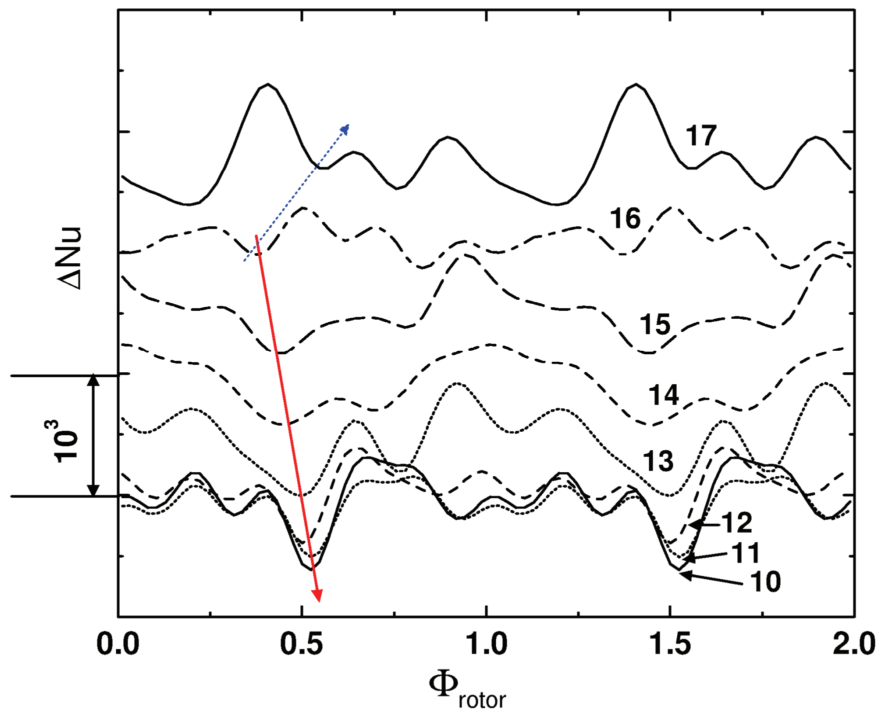

Figure 4-14: Most probable constant speed of the flow perturbations on the blade surface from position 16 till 10

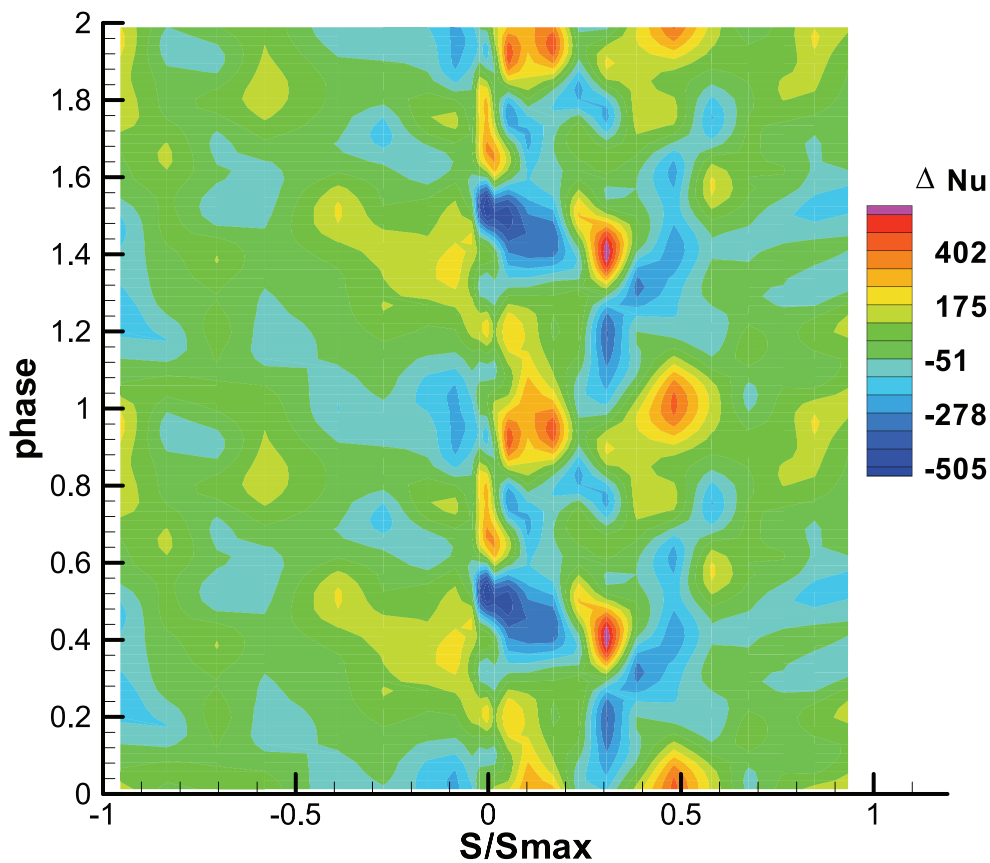

Figure 4-15: Contour map of the Nusselt number traces of the single-layer gauges at 50% span

The contour map of the Nusselt number traces of the single-layer gauges at 50% span in Figure 4-15 is another representation of the information shown in Figure 4-13. The movement of the flow perturbations upstream and downstream of the area of the gauges 15, 16 17 at the suction side of the second stator vane is obvious.

The results from the measurements with the single-layer gauges on the second stator of the CT3 facility are also published by Iliopoulou et al. (2004).

4.6.3 Random unsteadiness

The *RMS* is proportional to the level of the unsteadiness of the measured value, which is the Nusselt number in our case. It is expected that at the location where the flow perturbations imping on the second stator vanes, the unsteadiness on the Nusselt number is higher. (More specifically, the peak in *RMS* stems from the slight changes of the peak in the Nusselt number fluctuations.) In Figure 4-16, the unsteady *RMS* traces of the Nusselt number at 50% span from one representative test are plotted over two blade-passing periods.

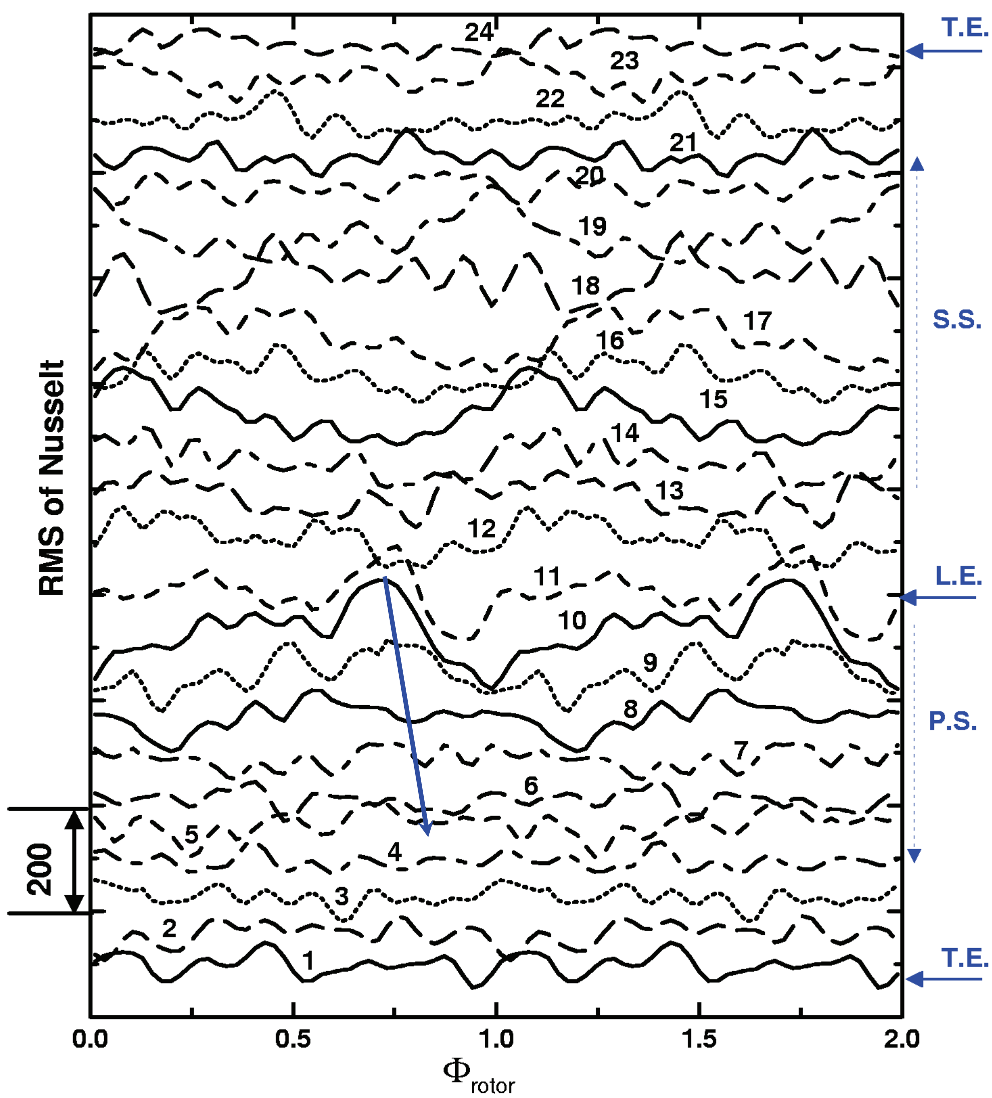

Figure 4-16: Unsteady *RMS* traces of the Nusselt number at 50% span from the experiment 51 of the single-layer gauges

The gauges that are close to the stagnation region (gauges 209, 210, 211, 213, 214) have a noticeable higher value on the *RMS* (indicated with an arrow), in comparison to the rest of the gauges of the same test. The relative time to the phase of the rotor that corresponds to these higher values of the *RMS* is comparable to the same relative time that corresponds to higher values of the Nusselt number *PLA* in Figure 4-13.

Thus, the *RMS* signal of the Nusselt number does not give additional information about the phenomena of the flow field, but indicates the regions with high unsteadiness. The difficulty with the signal of the gauges is that it suffers from noise much more than the pressure transducers (Gadea et al., 2004). When this noise exceeds few tenths of millivolts, it can introduce fluctuations on the measured signal even higher than the actual ones that are coming from the unsteadiness of the flow field.

In order to give an estimation of the repeatability, the unsteady *RMS* traces of the Nusselt number of gauge 211 of five different tests for the single-layer gauges are given in Figure 4-17. The gauge 211 is selected, because of the observation of the highest RMS level in comparison to the rest of the gauges. The repeatability for this gauge is good.

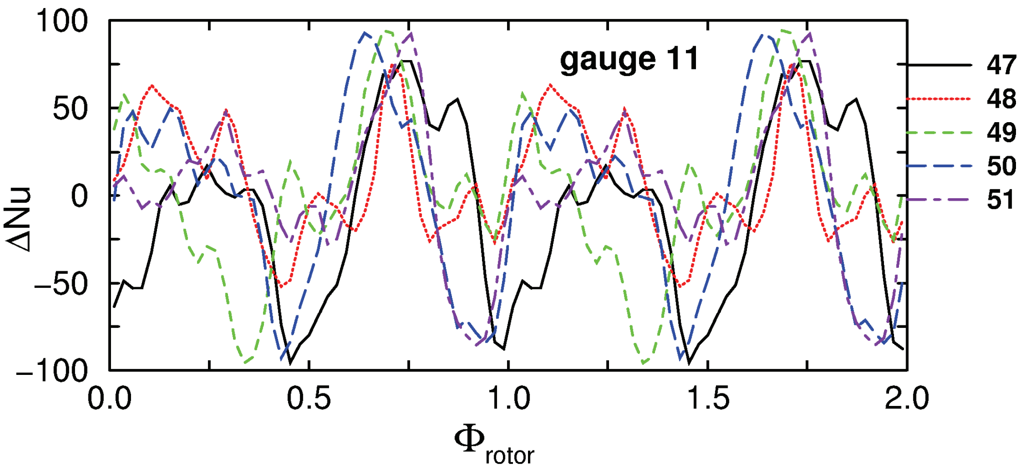

Figure 4-17: Unsteady *RMS* traces of the Nusselt number of gauge 11 of five different measurements for the single-layer gauge

4.7 References

Ainsworth R.W., Allen J.L., Davies M.R.D., Doorly J.E., Forth C.J.P, Hilditch M.A., Oldfield M.L.G., Sheard A.G., 1989, *'Developments in Instrumentation and Processing for Transient Heat Transfer Measurement in a full-Stage Model Turbine'*, J. of Turbomachinery, vol. 111, pp 20-27

Arts T., 1994, *'Measurement chain: definitions, error and uncertainty'*, Measurement Techniques in Fluid Dynamics, VKI LS 1994-01, ISBN D/1994/0238/417

Arts T., Lambert de Rouvroit M., and Rutherford A.W., 1990, *'Aero-thermal investigation of a highly loaded transonic linear turbine guide vane cascade (A test case for inviscid and viscous flow computations)'*, VKI TN 174.

Denos R., 1996, *'Aerothermal investigation of the unsteady flow in the rotor of a transonic turbine stage'*, Ph.D. thesis, University of Poitiers, France

Denos R., Arts T., Paniagua G., Michelassi V., Martelli F., 2001, *'Investigation of the unsteady rotor aerodynamics in a transonic turbine stage'*, J. of Turbomachinery, vol. 123 (1), pp 81-89

Ferrara F., 2002, *'Assessment of a heat flux source for the determination of thin film gauge substrate thermal product'*, VKI SR 2002-15

Gadea J., Denos R., Paniagua G., Billiard N., Sieverding C.H., 2004, *'Effect of clocking on the second stator pressure field of a one and a half stage transonic turbine'*, ASME GT2004-53463, Vienna, Austria

Iliopoulou V., Denos R., Billiard N., Arts T., 2004, *'Time averaged and time-resolved heat flux measurements on a turbine stator blade using two-layered thin-film gauges'*, ASME 2004-GT-53437, Vienna, Austria – J. of Turbomachinery, vol. 126, pp 570-577

Paniagua G., Denos R., Arts T., 2001, *'Steady-unsteady measurements of the flow field downstream of a transonic high-pressure turbine stage'*, Proc. of the Inst. of Mech Engrs, vol. 215 (A) pp 663-673